Precise GNSS Positioning with Time-differenced Carrier Phases at Variable Sampling Rates

Shuai Guo [1], Hongzhou Yang [1], Yang Gao [1]

[1] Dept. of Geomatics Engineering, University of Calgary, Calgary, AB, Canada – honyang@ucalgary.ca

Keywords: GNSS, Variable Sampling Rates, SDR, TDCP, Dynamic Navigation.

Abstract

Most Global Navigation Satellite System (GNSS) receivers typically have a sampling rate at 1Hz. However, variable sampling rates are required for optimal performance in different dynamic applications. For example, high sampling rates are crucial for precise tracking of high dynamic platforms such as unmanned aerial vehicle (UAV) navigation. Higher sampling rates help decrease positioning interval time and improve travel distance measurements especially when moving on a curvy route. On the contrary, lower sampling rates help saving power consumption and computation. Currently there is barely literature presenting the impact of sampling rates on positioning accuracy and what sampling rate is required for different vehicle dynamics considering the positioning accuracy and computational load. In this study, we extend TDCP to estimate position at different sampling rates and with high accuracy. We investigate and develop a GNSS software-defined radio (SDR) receiver to implement variable sampling-rate capability at low-cost. This approach provides flexibility, customization and scalability since the GNSS SDR can be reconfigured or updated via software to support multiple GNSS signals, systems or new techniques without requiring costly hardware modifications. The variable-rate phase observations from the GNSS SDR will be applied to form time-differenced carrier phase (TDCP) observations for precise positioning. The test results show that the GNSS-TDCP algorithm can achieve absolute precise positioning, but the positioning error will drift over time. Besides, the research results on the impact of different sampling rates on the positioning performance can help us to select an appropriate sampling rate for GNSS-TDCP system.

1. Introduction

Precise positioning is important for many dynamic applications such as land vehicles, unmanned aerial vehicles (UAV), smart phones, and mobile robotics (Grayson et al., 2018). The Inertial Measurement System (INS) and the Global Navigation Satellite System (GNSS) are two widely used positioning systems. INS consists of the inertial measurement unit (IMU) and computational unit. IMU is typically made up of a 3-axis accelerometer and a 3-axis gyroscope to measure the system's angular rate and acceleration (EI-Sheimy & Youssef, 2020). Using raw measurements from the IMU, the computational unit used to continuously calculate the position, velocity and attitude of the system by dead reckoning (Niu et al., 2021). GNSS technology is a very effective way to get accurate position. Single Point Positioning (SPP) is a GNSS positioning approach using pseudorange measurements to provide positioning accuracy at several meters (Medina et al., 2020). Real-Time Kinematic (RTK) positioning or Precise Point Positioning (PPP) are widely adopted for positioning tasks requiring much higher accuracy. Since RTK requires a fixed base station or access to a continuously operating reference station (CORS) network, it may not always be available, particularly in remote areas (Teunissen et al., 2010). Its accuracy also degrades with increase of distance from the base station due to the growing impact of atmospheric and signal propagation errors. PPP typically requires long time to converge to high-precision results because of ambiguity resolution (Tu et al., 2013). It also requires access to precise satellite clock and orbit corrections from external services such as the International GNSS Service (IGS) or commercial providers (Martin et al., 2011).

In recent years, we have witnessed increased research on time-differenced carrier phase (TDCP) based precise positioning since it does not rely on fixed base station or external correction services as the case in RTK and PPP techniques. By differencing the GNSS carrier phase measurements over time, the TDCP-based technique can cancel out the ionospheric delay, tropospheric delay, satellite clocks and orbit errors (Soon et al., 2008). TDCP technique can also overcomes carrier phase ambiguity problem (Sun et al., 2020). Because the ambiguity is constant in the case of no cycle slip and is cancelled out by differencing carrier phases between two consecutive time epochs (Freda et al., 2015). The TDCP observables are directly corresponding to the position increment and has been widely applied to estimate the velocity with high accuracy (Suzuki, 2022). However currently there is barely literature researching the impact of sampling rates on positioning accuracy and what sampling rate is required for different travel dynamics considering the positioning accuracy and computational load.

Most Global Navigation Satellite System (GNSS) receivers typically have a sampling rate at 1Hz (Lechner & Baumann, 2000). In recent years, major high-precision geodetic GNSS receiver manufacturers started to enable high sampling-rate capability, but they are usually too expensive for most users (Bischof & Schön, 2015). GNSS software-defined radio (SDR) receiver is a good choice to implement variable sampling-rate capability at low-cost. This approach provides flexibility, customization and scalability since the GNSS SDR can be reconfigured or updated via software to support multiple GNSS signals, systems or new techniques without requiring costly hardware modifications (Söderholm et al., 2016). GNSS SDR use general-purpose processors to reduce the need for specialized hardware, making prototyping and testing less expensive (Linty et al., 2018). With a GNSS-SDR, it captures raw radio frequency (RF) signals from GNSS satellites using a RF front-end, then convert to digital intermediate frequency (IF) signal. The software will get GNSS measurements from IF signal using acquisition and tracking algorithms (Kumar & Paidimarry, 2020). Additionally, the GNSS SDR allows adjusting the phase lock loop (PLL) parameters such as the bandwidth and the coherence integration time to influence the ability of the receiver to achieve high-rate positioning (Curran et al., 2012). A GNSS-TDCP algorithm at variable sampling rates can be implemented on a GNSS-SDR to evaluate the impact of sampling rate on positioning performance.

2. Methods

2.1 TDCP technique for relative positioning

The carrier phase measurements are the phase difference between satellites and receivers and its measurement model can be written as follows:

$$\phi = \frac{1}{\lambda}\left(\rho_u^s + cdt_u - cdt^s - I_\phi + T_\phi\right) + N + \varepsilon_\phi \tag{1}$$

where:

ϕ is the carrier phase measurement in cycles.
λ is the carrier wavelength.
ρ_u^s is the geometric range between the satellite and the receiver antenna.
c is the speed of light in a vacuum.
dt_u is the receiver clock bias.
dt^s is the satellite clock bias.
I_ϕ is the ionospheric delay.
T_ϕ is the tropospheric delay.
N is the carrier phase integer ambiguity in cycles.
ε_ϕ is the measurement errors of carrier phase.

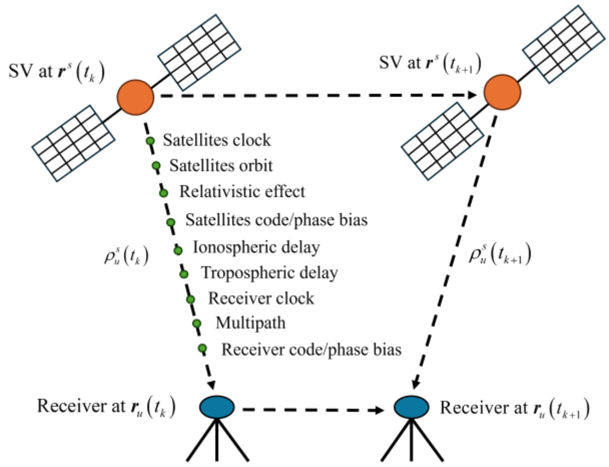

Figure 1. Relative satellite-receiver geometry between two epochs

Figure 1 shows the motion of the GNSS satellite and antenna at two successive epochs. Because of the existence of the carrier phase integer ambiguity, integer ambiguity resolution is necessary for positioning to get fixed solution instead of float solution. TDCP observation ns however can eliminate integer ambiguity by between-time differencing. Let the carrier phase measurement equation at epoch t_k expressed as follows:

$$\begin{aligned}\phi(t_k) = &\frac{1}{\lambda}\left[\rho_u^s(t_k) + cdt_u(t_k) - cdt^s(t_k)\right] + \\ &\frac{1}{\lambda}\left[-I_\phi(t_k) + T_\phi(t_k)\right] + N(t_k) + \varepsilon_\phi(t_k)\end{aligned} \tag{2}$$

and the carrier phase measurement equation at epoch t_{k+1} as follows:

$$\begin{aligned}\phi(t_{k+1}) = &\frac{1}{\lambda}\left[\rho_u^s(t_{k+1}) + cdt_u(t_{k+1}) - cdt^s(t_{k+1})\right] + \\ &\frac{1}{\lambda}\left[-I_\phi(t_{k+1}) + T_\phi(t_{k+1})\right] + N(t_{k+1}) + \varepsilon_\phi(t_{k+1})\end{aligned} \tag{3}$$

The difference between two successive carrier phase measurements at epochs t_{k+1} and t_k can be calculated as follows:

$$\begin{aligned}\Delta\phi &= \phi(t_{k+1}) - \phi(t_k) \\ &= \frac{1}{\lambda}\left(\Delta\rho_u^s + c\Delta dt_u - c\Delta dt^s - \Delta I_\phi + \Delta T_\phi\right) + \Delta\varepsilon_\phi\end{aligned} \tag{4}$$

where Δ represents the differencing operation. Between two successive epochs, The carrier phase integer ambiguity $N(t_k)$ is equal to $N(t_{k+1})$ when the cycle slip is handled, the difference of the satellite clock bias Δdt^s, the ionospheric delay ΔI_ϕ, and the tropospheric delay ΔT_ϕ vary slowly which approximated at zero. Therefore, the TDCP measurement can be written as:

$$\Delta\phi = \frac{1}{\lambda}\left(\Delta\rho_u^s + c\Delta dt_u\right) + \Delta\varepsilon_\phi \tag{5}$$

The geometric range between the satellite and the receiver antenna can be formulated as follows:

$$\begin{cases}\rho_u^s(t_k) = \boldsymbol{e}(t_k)\cdot\left[\boldsymbol{r}^s(t_k) - \boldsymbol{r}_u(t_k)\right] \\ \rho_u^s(t_{k+1}) = \boldsymbol{e}(t_{k+1})\cdot\left[\boldsymbol{r}^s(t_{k+1}) - \boldsymbol{r}_u(t_{k+1})\right]\end{cases} \tag{6}$$

where $\boldsymbol{r}^s$ is the satellite position. $\boldsymbol{r}_u$ is the receiver position. $\boldsymbol{e}$ is the line-of-sight unit vector which can be calculated as follows:

$$\begin{cases}\boldsymbol{e}(t_k) = \dfrac{\boldsymbol{r}^s(t_k) - \boldsymbol{r}_u(t_k)}{\left\|\boldsymbol{r}^s(t_k) - \boldsymbol{r}_u(t_k)\right\|} \\ \boldsymbol{e}(t_{k+1}) = \dfrac{\boldsymbol{r}^s(t_{k+1}) - \boldsymbol{r}_u(t_{k+1})}{\left\|\boldsymbol{r}^s(t_{k+1}) - \boldsymbol{r}_u(t_{k+1})\right\|}\end{cases} \tag{7}$$

Therefore, the term $\Delta\rho_u^s$ in equation (5) can be expressed as follows:

$$\begin{aligned}\Delta\rho_u^s &= \rho_u^s(t_{k+1}) - \rho_u^s(t_k) \\ &= \boldsymbol{e}(t_{k+1})\cdot\left[\boldsymbol{r}^s(t_{k+1}) - \boldsymbol{r}_u(t_{k+1})\right] \\ &\quad - \boldsymbol{e}(t_k)\cdot\left[\boldsymbol{r}^s(t_k) - \boldsymbol{r}_u(t_k)\right] \\ &= \left[\boldsymbol{e}(t_{k+1})\cdot\boldsymbol{r}^s(t_{k+1}) - \boldsymbol{e}(t_k)\cdot\boldsymbol{r}^s(t_k)\right] \\ &\quad - \left[\boldsymbol{e}(t_{k+1})\cdot\boldsymbol{r}_u(t_{k+1}) - \boldsymbol{e}(t_k)\cdot\boldsymbol{r}_u(t_k)\right]\end{aligned} \tag{8}$$

Besides, the receiver position at epoch t_{k+1} and epoch t_k can be expressed as follows:

$$\boldsymbol{r}_u(t_{k+1}) = \boldsymbol{r}_u(t_k) + \Delta\boldsymbol{r}_u \tag{9}$$

where $\Delta\boldsymbol{r}_u$ is the receiver position change between t_{k+1} and t_k.

Substituting equation (9) in (8):

$$
\begin{aligned}
\Delta\rho_u^s &= \left\{ \boldsymbol{e}(t_{k+1}) \cdot \boldsymbol{r}^s(t_{k+1}) - \boldsymbol{e}(t_k) \cdot \boldsymbol{r}^s(t_k) \right\} \\
&\quad - \left\{ \boldsymbol{e}(t_{k+1}) \cdot \left(\boldsymbol{r}_u(t_k) + \Delta\boldsymbol{r}_u \right) - \boldsymbol{e}(t_k) \cdot \boldsymbol{r}_u(t_k) \right\} \\
&= \left\{ \boldsymbol{e}(t_{k+1}) \cdot \boldsymbol{r}^s(t_{k+1}) - \boldsymbol{e}(t_k) \cdot \boldsymbol{r}^s(t_k) \right\} \\
&\quad - \left\{ \boldsymbol{e}(t_{k+1}) \cdot \boldsymbol{r}_u(t_k) - \boldsymbol{e}(t_k) \cdot \boldsymbol{r}_u(t_k) + \boldsymbol{e}(t_{k+1}) \cdot \Delta\boldsymbol{r}_u \right\}
\end{aligned}
\tag{10}
$$

The equation (5) can be written as:

$$
\begin{aligned}
&\Delta\phi - \frac{1}{\lambda}\left[\boldsymbol{e}(t_{k+1}) \cdot \boldsymbol{r}^s(t_{k+1}) - \boldsymbol{e}(t_k) \cdot \boldsymbol{r}^s(t_k) \right] + \\
&\frac{1}{\lambda}\left[\boldsymbol{e}(t_{k+1}) \cdot \boldsymbol{r}_u(t_k) - \boldsymbol{e}(t_k) \cdot \boldsymbol{r}_u(t_k) \right] \\
&= -\frac{1}{\lambda} \boldsymbol{e}(t_{k+1}) \cdot \Delta\boldsymbol{r}_u + \frac{c}{\lambda}\Delta dt_u + \Delta\varepsilon_\phi
\end{aligned}
\tag{11}
$$

Let the left part of the equation (11) equal to $\Delta\tilde{\phi}$. Equation (11) can be rewritten in the vector form:

$$
\begin{bmatrix} -\boldsymbol{e}(t_{k+1}) & 1 \end{bmatrix} \begin{bmatrix} \Delta\boldsymbol{r}_u \\ c\Delta dt_u \end{bmatrix} = \lambda\Delta\tilde{\phi} + \lambda\Delta\varepsilon_\phi \tag{12}
$$

Using the Least Squares (LS) method, the receiver position change and the receiver clock bias error between t_{k+1} and t_k can be estimated by:

$$
\boldsymbol{x} = \left(\boldsymbol{G}^T \boldsymbol{G} \right)^{-1} \boldsymbol{G}^T \boldsymbol{y} \tag{13}
$$

where,

$$
\boldsymbol{x} = \begin{bmatrix} \Delta r_u^x \\ \Delta r_u^y \\ \Delta r_u^z \\ c\Delta dt_u \end{bmatrix} \tag{14}
$$

$$
\boldsymbol{G} = \begin{bmatrix} -\boldsymbol{e}_1^x(t_{k+1}) & -\boldsymbol{e}_1^y(t_{k+1}) & -\boldsymbol{e}_1^z(t_{k+1}) & 1 \\ -\boldsymbol{e}_2^x(t_{k+1}) & -\boldsymbol{e}_2^y(t_{k+1}) & -\boldsymbol{e}_3^z(t_{k+1}) & 1 \\ & \vdots & & \\ -\boldsymbol{e}_m^x(t_{k+1}) & -\boldsymbol{e}_m^y(t_{k+1}) & -\boldsymbol{e}_m^z(t_{k+1}) & 1 \end{bmatrix} \tag{15}
$$

$$
\boldsymbol{y} = \begin{bmatrix} \lambda\Delta\tilde{\phi}_1 \\ \lambda\Delta\tilde{\phi}_2 \\ \vdots \\ \lambda\Delta\tilde{\phi}_m \end{bmatrix} \tag{16}
$$

and Δr_u^x, Δr_u^y, and Δr_u^z are displacement increments in the ECEF frame between two successive epochs. Therefore, the absolute position can be obtained by accumulating displacement increments over time since initial position. m is the number of satellites.

2.2 GNSS-SDR for implementing TDCP

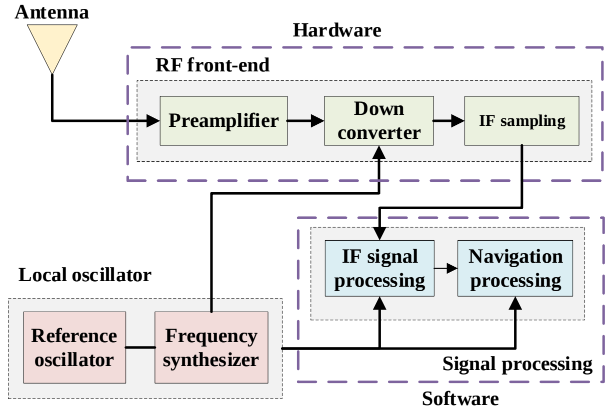

Figure 2. Block diagram of the GNSS software receiver

As shown in Figure 2, a GNSS SDR consists of the local oscillator, the RF front-end section, and the IF signal processing section. The downconverter transforms RF to IF which will be used in signal processing section. The local oscillator provides GNSS receivers basic unit of timing by the reference oscillator. The IF signal processing consists of the acquisition and the tracking. The acquisition can get coarse carrier and code phase parameters, which includes several methods, like, 1) the serial search acquisition, 2) the parallel frequency space search acquisition, 3) the parallel code phase search acquisition. The tracking is to get accurate carrier and code phase, which includes two steps: 1) the carrier tracking, 2) the code tracking. The navigation processing can calculate position, velocity, and time from pseudorange, phase, and Doppler measurements generated by the IF signal processing.

3. Experiment and Results

In this section, a vehicle-based kinematic test is conducted to validate the performance of the variable sampling-rate TDCP based positioning algorithm. The speed of the vehicle is about 60km/h. We use the TDCP technique as dead-reckoning to get absolute position and investigate the position error drifting problem. In the field test, a Novatel GPS-703-GGG antenna and a NUT2NT+ RF front-end are used to obtain intermediate frequency (IF) data which can be processed by a GNSS SDR. The positioning ground truth will be generated by the RTK solutions from a NovAtel SPAN system. Devices for the test are shown in Figure 3.

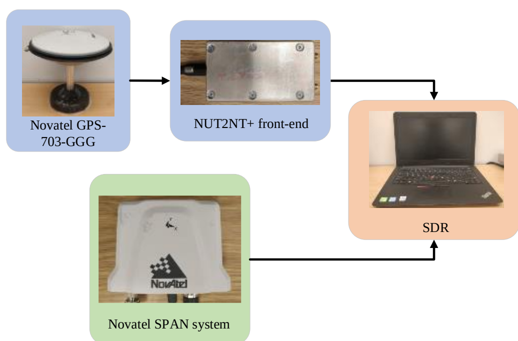

Figure 3. Devices for testing the proposed algorithm.

We implement TDCP positioning technique in a GNSS SDR platform developed at the Positioning and Mobile Information (PMIS) research group at The University of Calgary and tested with the sampling rates at 1/60 Hz, 1/40 Hz, 1/30 Hz, 1/20 Hz, 1/10 Hz, 1 Hz, 10 Hz, 20 Hz, and even reach 50 Hz, 100 Hz, respectively. High sampling rates such as 10 Hz, 20 Hz, 50 Hz, and 100 Hz are used to cope with high vehicle dynamics. Low sampling rates such as 1/10 Hz, 1/20 Hz, and 1 Hz are used to cope with low vehicle dynamics. The trajectory for 240 s of ground truth (GT) got by SPAN system is shown in figure 4. The test was done in an open-sky scenario. The initial position of GNSS-TDCP system is provided by GT. Then TDCP is used to get displacement increments.

Figure 4. The ttrajectory of SPAN system

To analyse the influence of sampling rates on positioning errors, we process the same data for 240 s with different sampling rates. We take the positioning results at 10 Hz as an example. The horizontal trajectory of GT, and GNSS-TDCP in the East-North horizontal for 240 s at 10 Hz sampling rate are presented in Figure 5. The enlarged image gives the details for the end of the motion segment, which is marked by the blue rectangle. GNSS-TDCP position closely follows GT with minimal deviation.

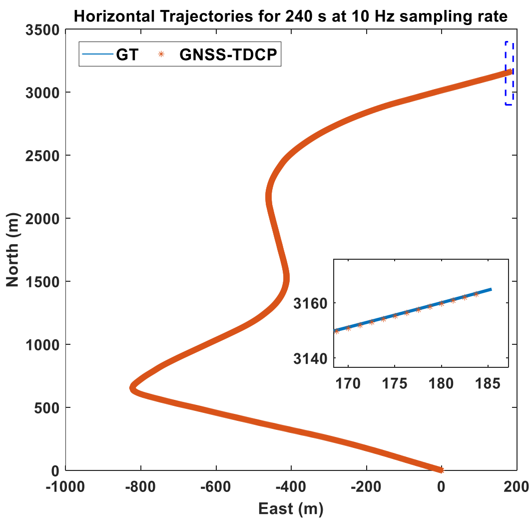

Figure 5. Horizontal trajectories for 240 s at 10 Hz sampling rate

Figure 6 shows the power spectral density (PSD) of displacement increments errors at 10 Hz sampling rate in the East, North, and Up directions. The PSD of displacement increments errors basically appears as flat lines within the frequency range. It indicates the displacement increments errors is the white noise. Because the energy of white noise distributes uniformly across all frequencies, its PSD curve is a horizontal straight line throughout the entire frequency range.

Figure 7 shows the probability density function (PDF) of displacement increments errors at 10 Hz sampling rate in the East, North, and Up directions. Displacement increments errors can be considered as mainly containing Gaussian white noise because these PDFs basically follow Gaussian distribution. Therefore, as an integral of Gaussian white noise, absolute positioning errors follow a random walk.

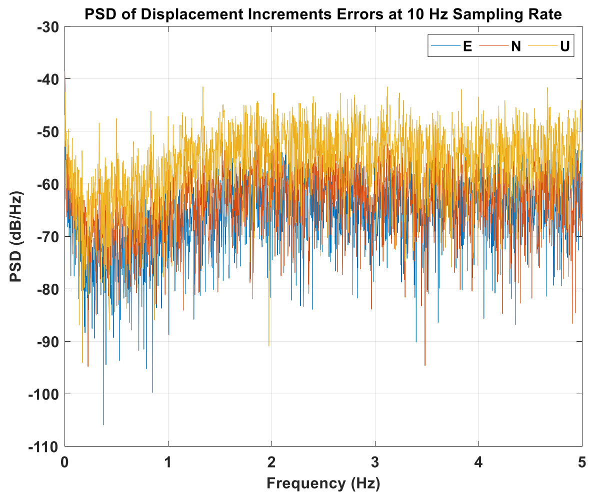

Figure 6. PSD of displacement increments errors at 10 Hz sampling Rate

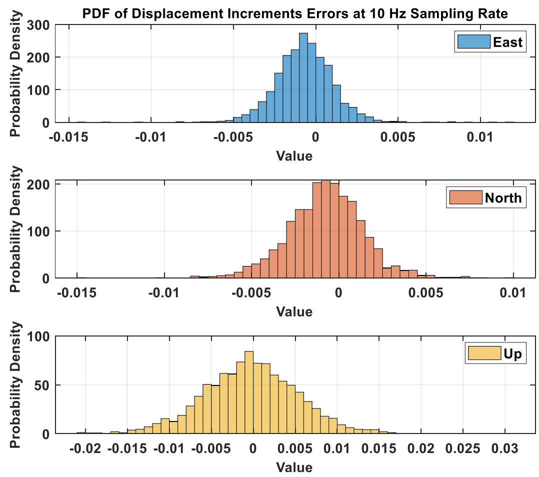

Figure 7. PDF of displacement increments errors at 10 Hz sampling rate

Figure 8 presents GNSS-TDCP positioning errors at different sampling rates in East, North, and Up direction. Positioning errors have the same trend at different sampling rates, which follow the random walk. The results indicate positioning errors drift over time because absolute positions are accumulated by displacement increments computed by TDCP. Positioning errors accumulate gradually and stay within 2 m throughout the 240 s test period. Because TDCP can cancel out ionospheric delay errors, tropospheric delay errors, satellite clocks errors and orbit errors, high-accuracy displacement increments can be provided by TDCP.

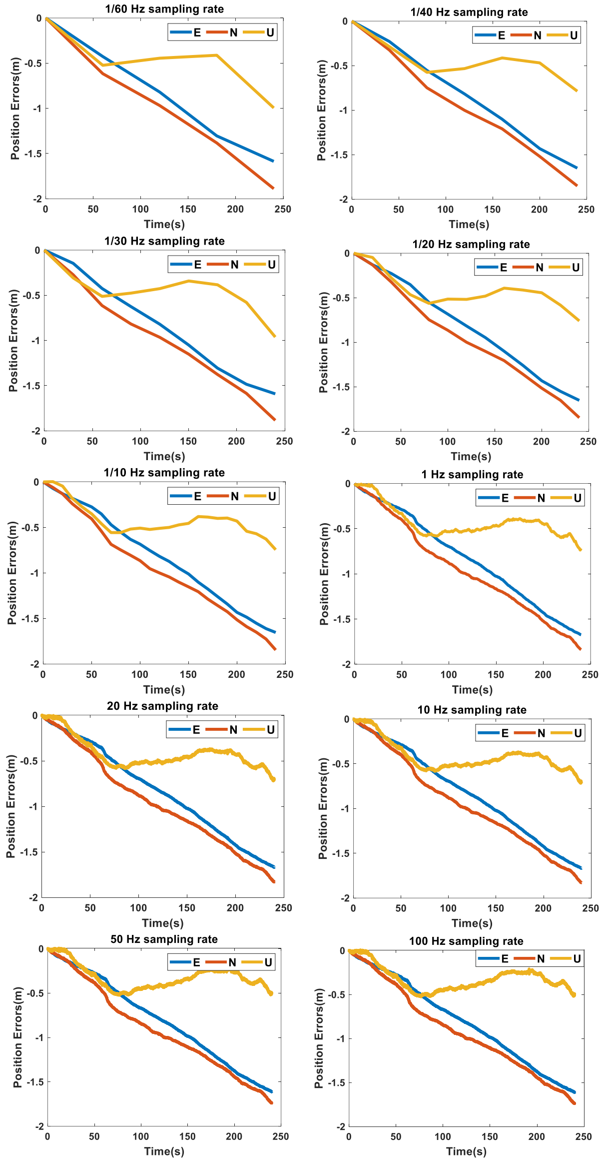

Figure 8. GNSS-TDCP positioning errors at different sampling rates

The results of positioning errors in terms of RMS at different sampling rates are shown in Table 1. RMS values also be plotted in Figure 9 in East, North, and Up direction. The RMS of positioning errors increase slightly with the increase of sampling rate. Besides, the RMS of positioning errors basically does not change between the sampling rate 10 Hz and 20 Hz, 50 Hz and 100 Hz. Even as the sampling rate increases, TDCP can increasingly eliminate ionospheric delay errors, tropospheric delay errors, satellite clock errors, and orbital errors between two consecutive epochs more effectively. But the overall error remains the same for a period. Therefore, it is not cost-effective to increase the sampling frequency to improve the positioning performance, but high sampling rate will increase computation consumption. Besides, increasing the sampling rate cannot continuously improve the performance of the GNSS-TDCP algorithm. The GNSS-TDCP system can select a high sampling rate to increase the update rate to match the speed in high-speed motion scenarios. But it must balance the accuracy and power consumption to get optimal performance. In low-speed motion scenarios, it is a good choice to use low sampling rate for the GNSS-TDCP system.

Table 1. RMS of positioning errors at different sampling rates

Sampling rate (Hz)	RMS of positioning errors (m)		
	East	North	Up
1/60	1.007	1.166	0.571
1/40	1.001	1.126	0.494
1/30	0.989	1.122	0.505
1/20	0.981	1.098	0.466
1/10	0.972	1.087	0.455
1	0.969	1.085	0.458
10	0.965	1.079	0.447
20	0.965	1.079	0.447
50	0.931	1.028	0.348
100	0.931	1.028	0.348

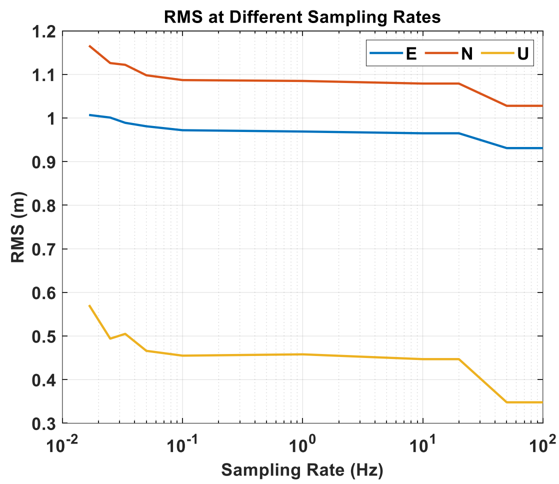

Figure 9. RMS of positioning errors at different sampling rates

4. Conclusions and Future Work

In this paper, a GNSS-TDCP algorithm with variable sampling rates is implemented on GNSS-SDR platform. The influence of sampling rates on positioning accuracy is evaluated by theorical development and field tests. The test results show that TDCP can be used to achieve absolute precise positioning by cancelling out the ionospheric delay errors, tropospheric delay errors, satellite clock errors and orbit errors, but with drifting over time. Besides, high sampling rates can slightly help the GNSS-TDCP system reducing positioning errors which within 2m for 240s operating at sampling rate but have a limitation. Because the overall errors remain the same for a period. An appropriate sampling rate should be select to make the GNSS-TDCP system achieve optimal performance. In high-speed motion scenarios, The GNSS-TDCP system can select a high sampling to increase the update rate to match the speed. However, in low-speed or discontinuous positioning motion scenarios, the GNSS-TDCP system can use a lower sampling rate to reduce computational complexity while obtaining high-precision positioning solution. The GNSS-TDCP system is also a good choice to provide a high precise initial position for PPP and RTK.

In the future work, we will do more tests to research on the relationship between sampling rate and the dynamic. We will also use the UAV to do quick acceleration, braking, and turning motions to test in high dynamics from the perspectives of acceleration. Both IF data and IMU data will be collected in all tests. IF data collected by the front-end will be processed by our GNSS SDR using the proposed TDCP positioning technique with the variable sampling rates. These results will be compared with the INS results for dead reckoning performance. We expect to present the relationship between the dynamic and sampling rates, which can evaluate the impact of the sampling rates on the positioning accuracy and guide us to select the optimal sampling rate for different dynamic applications.

Acknowledgements

The financial support from the Chinese Scholarship Council (CSC) are greatly acknowledged.

References

Grayson, B., Penna, N.T., Mills, J.P., Grant, D.S., 2018. GPS precise point positioning for UAV photogrammetry. *The photogrammetric record*, 33(164), 427-447.

El-Sheimy, N., Youssef, A., 2020. Inertial sensors technologies for navigation applications: State of the art and future trends. *Satellite Navigation*, 1(1), 2.

Niu, X., Wu, Y., Kuang, J., 2021. Wheel-INS: A wheel-mounted MEMS IMU-based dead reckoning system. *IEEE Transactions on Vehicular Technology*, 70(10), 9814-9825.

Medina, D., Ortega, L., Vilà-Valls, J., Closas, P., Vincent, F., Chaumette, E., 2020. Compact CRB for delay, Doppler, and phase estimation–application to GNSS SPP and RTK performance characterisation. *IET Radar, Sonar & Navigation*, 14(10), 1537-1549.

Teunissen, P.J., Odijk, D., Zhang, B., 2010. PPP-RTK: results of CORS network-based PPP with integer ambiguity resolution. *J Aeronaut Astronaut Aviat Ser A*, 42(4), 223-230.

Tu, R., Ge, M., Zhang, H., Huang, G., 2013. The realization and convergence analysis of combined PPP based on raw observation. *Advances in space research*, 52(1), 211-221.

Martín, A., Anquela, A.B., Capilla, R., Berné, J.L., 2011. PPP technique analysis based on time convergence, repeatability, IGS products, different software processing, and GPS+ GLONASS constellation. *Journal of Surveying Engineering*, 137(3), 99-108.

Soon, B.K., Scheding, S., Lee, H.K., Lee, H.K., Durrant-Whyte, H., 2008. An approach to aid INS using time-differenced GPS carrier phase (TDCP) measurements. *GPS Solutions*, 12, 261-271.

Sun, R., Cheng, Q., Wang, J., 2020. Precise vehicle dynamic heading and pitch angle estimation using time-differenced measurements from a single GNSS antenna. *GPS Solutions*, 24, 1-9.

Freda, P., Angrisano, A., Gaglione, S., Troisi, S., 2015. Time-differenced carrier phases technique for precise GNSS velocity estimation. *GPS Solutions*, 19, 335-341.

Suzuki, T., 2022. GNSS odometry: Precise trajectory estimation based on carrier phase cycle slip estimation. *IEEE Robotics and Automation Letters*, 7(3), 7319-7326.

Lechner, W., Baumann, S., 2000. Global navigation satellite systems. *Computers and Electronics in Agriculture*, 25(1-2), 67-85.

Bischof, C., Schön, S., 2015. High-Rate GPS Velocity and Acceleration Determination in Highly Dynamic Flights. In *Proceedings of the 28th International Technical Meeting of the Satellite Division of The Institute of Navigation (ION GNSS+ 2015)*, 3069-3076.

Söderholm, S., Bhuiyan, M.Z.H., Thombre, S., Ruotsalainen, L., Kuusniemi, H., 2016. A multi-GNSS software-defined receiver: design, implementation, and performance benefits. *Annals of Telecommunications*, 71(7), 399-410.

Linty, N., Dovis, F., Alfonsi, L., 2018. Software-defined radio technology for GNSS scintillation analysis: bring Antarctica to the lab. *GPS Solutions*, 22(4), 96.

Kumar, B.P., Paidimarry, C.S., 2020. Improved real time GPS RF data capturing for GNSS SDR applications. *Gyroscopy and Navigation*, 11(1), 59-67.

Curran, J.T., Lachapelle, G., Murphy, C.C., 2012. Digital GNSS PLL design conditioned on thermal and oscillator phase noise. *IEEE Transactions on Aerospace and Electronic Systems*, 48(1), 180-196.